RSC Advances

PAPER

View Article Online
View Journal | View Issue

Cite this: *RSC Adv.*, 2022, **12**, 13535

Robust photocatalytic activity of two-dimensional h-BN/Bi_2O_3 heterostructure quantum sheets†

Jianwei Zhou, *[ab] Fangfang Duo,[a] Chubei Wang,[a] Liangliang Chu,[a] Mingliang Zhang[a] and Donglei Yan[b]

Herein, defect intrinsic hexagonal boron nitride (h-BN) quantum sheets (QS) and bismuth oxide (Bi_2O_3) QS were prepared from bulk materials by ball milling and solvent stripping, respectively. The h-BN/Bi_2O_3 heterostructure was fabricated *via* a facile self-assembly method. The structure and performance of samples were systematically characterized. As expected, the layered h-BN QS is tightly coated on the surface of Bi_2O_3 QS in a face-to-face stacking structure and interconnected by strong interface interactions. The introduction of h-BN QS can significantly enhance the separation efficiency of the photogenerated carriers of h-BN/Bi_2O_3. The experimental results show that the photocatalytic activity of h-BN/Bi_2O_3 is markedly improved. The first-order reaction rate constant of the 3wt%-BN/Bi_2O_3 sample is 3.2×10^{-2} min^{-1}, about 4.5 times that of Bi_2O_3 QS. By means of the active species capture test, it is found that the main oxidation species are holes (h^+), followed by hydroxyl radicals ($^{\bullet}OH$). Based on the surface charge transfer characteristics, the photogenerated carrier transfer and separation efficiency can be improved by coupling h-BN and a Bi_2O_3 semiconductor to the Schottky heterojunction, and the strong interaction between heterogeneous interfaces also enhances the surface catalytic reaction efficiency, which improves dramatically the photocatalytic performance.

Received 15th March 2022
Accepted 27th April 2022

DOI: 10.1039/d2ra02115c

rsc.li/rsc-advances

1. Introduction

The problems associated with pollution and energy production have arisen along with the rapid development of industry and society, and have become the two main global challenges facing us today. The sustainable supply of clean and safe water is an essential guarantee of human life and health. In recent years, photocatalytic advanced oxidation technology has been considered a promising method for the degradation of organic pollutants due to the production of efficient active free radicals. Therefore, catalysts with high visible-light response and their applications have been attracted extensive attention.[1] A series of novel photocatalysts have been prepared and applied to the photo-induced chemical transformation reactions.[2–6] The photogenerated carriers can migrate to the catalyst surface and initiate chemical reactions in the process of photocatalysis, and have been used in the fields of pollutant degradation, water decomposition, air purification and disinfection.[7–9] However, the main challenges in the application of traditional semiconductor photocatalysts include insufficient utilization of sunlight, and high carrier recombination rate.[10,11] Therefore, it is urgent to develop novel catalytic materials with high light collection efficiency, high charge transfer efficiency and high chemical stability over the whole solar spectrum to accelerate the reaction.

Hexagonal boron nitride (h-BN) nanosheet structure has the characteristics of wide band gap, non-toxicity, high thermal conductivity and high specific surface area, which is used as holes transfer promoter in the process of semiconductor photocatalytic reaction, and can add attractive characteristics to photocatalysts.[12–15] In recent years, after combining with h-BN, the photocatalytic performance of semiconductors will be improved. Thus, many encouraging achievements have been achieved in h-BN based photocatalytic composites.[16–22] The enhanced catalytic performance is usually attributed to the promotion of photogenerated carriers transfer and migration rate, the inhibition of e^-–h^+ pairs recombination, the expansion of light response range and the increase of active sites of surface adsorbed reactants.[23,24] However, there is still a lack of strong theoretical analysis and experimental evidence. Indeed, the structure of BN plays an important role in BN/semiconductor heterostructures, but its inherent semiconductor characteristics and band gap adjustment are often ignored.[25,26]

Two-dimensional (2D) material has been widely investigated owning to their unique properties in electronics, optics, thermotics, catalysis and so on.[27] As the lateral size of 2D nanomaterial down to sub-20 nm regime, two-dimensional

[a]*Henan Photoelectrocatalytic Material and Micro-Nano Application Technology Academician Workstation, Xinxiang University, Xinxiang, Henan, China. E-mail: jwchow@163.com; Fax: +86-373-3682028; Tel: +86-373-3682028*

[b]*College of Chemistry and Material Engineering, Xinxiang University, Xinxiang 453003, PR China*

† Electronic supplementary information (ESI) available. See https://doi.org/10.1039/d2ra02115c

quantum sheets (2D QS) have appeared.[28] 2D QS has recently attracted more and more attention due to the integration of the inherent characteristics, quantum confinement and prominent edge effects of 2D materials.[29] The beauty of two-dimensional materials is that the material behavior is dominated *via* the interfaces. Therefore, interface interaction is the main consideration in the design of heterostructures, which directly determines the performance of the final device.[30] Bi_2O_3 semiconductor (E_g = ~2.7 eV) have a non-layered crystal structure and 3D intrinsic isotropic chemical bonds. Considering the creation of two-dimensional geometric Bi_2O_3 QS from bulk Bi_2O_3 materials may offer significant impact on catalyst design. Firstly, Bi_2O_3 QS may have large structural deformation and produce a large number of surface hanging bonds, which can achieve highly chemically active sites and enhance catalytic properties. Second, the structure and electronic properties of Bi_2O_3 QS can be adjusted by structure and surface engineering to further tuned the catalytic performance. Third, the exposed surface atoms with low coordination numbers can induce rapid interfacial carriers transfer and promote the chemisorption of reactants. In addition, defects will have additional effects on the surface electronic structure and charge transfer characteristics of semiconductors.[31] Meanwhile, the significant catalytic activity of Bi_2O_3 films is related to the existence of different oxidation states of Bi and the high oxygen mobility on the surface.[32] Many recent advances in the heterostructure of 2D materials have opened new routes and possibilities in catalysis field, such as TNS/WS_2,[33] Fe_2O_3/g-C_3N_4,[34] h-BN/BiOCl[35] and so on. In general, van der Waals junctions have weak bonding force and may not be suitable for building energy conversion devices.[36–38] According to literature reports, relatively tightly bonded 2D–2D heterojunctions have been successfully prepared,[39,40] but the preparation process is generally complicated and difficult to extend its application.

In this study, employing low-cost raw bulk precursors, a novel 2D h-BN/Bi_2O_3 heterostructure has been prepared by *ex situ* self-assembly of Bi_2O_3 QS and h-BN QS. The effects of h-BN QS incorporating into the structure, surface chemistry and catalytic activity were systematically investigated. In addition, the unique photocatalytic performance and reactive mechanism are discussed, which will contribute to the design and fabrication of the high performance catalysts, establish reliable structure–activity relationships and promote the application of BN-based materials in environmental purification and energy conversion.

2. Experimental section

2.1 Materials

Hexagonal boron nitride (h-BN) and bismuth trioxide (Bi_2O_3) were purchased from Sinopharm Chemical Reagent Co., Ltd. *N*-Methyl-2-pyrrolidone (NMP) was purchased from Shanghai Macklin Biochemical Co., Ltd. Acetate ether ($C_5H_{10}O_3$), ethanol (C_2H_5OH), sodium chloride (NaCl), were purchased from Beijing Chemical Works. All of reagents were used as received. Deionized water was used in the experiments.

2.2 Preparation of h-BN and Bi_2O_3 quantum sheets

Herein, h-BN QS and Bi_2O_3 QS were prepared by sequential combination of salt assisted ball milling and ultrasonic assisted solvent exfoliation of corresponding bulk materials. Briefly, a certain quality of sample and NaCl was mixed and put into agate ball milling tank, and ball milled at 350 rpm for 12 h (Planetary ball mill, QM-1SP4, Nanjing University Instrument Factory). Then, the powder mixture was washed with water until there was no precipitation in the filtrate when $AgNO_3$ is added. The dried filter cake was then dispersed in NMP solution for sonication (KQ-250DE, Kunshan Ultrasonic Instruments Co., Ltd) at 250 W for 4 h. When a certain amount of acetate ether was added, the solid phase could be completely precipitated from the dispersion.

And then, the dispersion was centrifuged (L550, Xiangyi Centrifuge Instrument Co., Ltd) at 4000 rpm for 20 min. After vacuum drying, the quantum sheet powders were collected.

2.3 Construction of h-BN/Bi_2O_3 heterostructures

The h-BN/Bi_2O_3 composites were synthesized *via* a facile electrostatic self-assembly approach. Driven by electrostatic attraction, components with opposite surface charges can be easily assembled into heterojunctions.[41] Briefly, under magnetic agitation, a certain amount of Bi_2O_3 QS was dispersed in absolute ethanol. Subsequently, different amounts of h-BN QS were added into the above suspension stirring for 3 h. Then, a homogenous suspension was obtained after sonicating for 3 h. The resultant suspension was centrifuged and dried at 60 °C overnight. The obtained h-BN/Bi_2O_3 composites with different h-BN weight ratios were denominated as 1%-BN/Bi_2O_3, 3%-BN/Bi_2O_3 and 5%-BN/Bi_2O_3, respectively.

2.4 Characterization

X-ray diffractometer (XRD, Bruker D8 Advance) was used to characterize the crystal structures. DRS spectra and IR spectra were identified on a Hitachi UV-3010 spectrophotometer and a Thermo iS50 FT-IR instrument, respectively. Photoluminescence (PL) spectra were recorded on a Hitachi F-4500 spectrofluorimeter, and the time-resolved photoluminescence (TRPL) decay spectra were recorded on a FLS 980 fluorescence spectrometer (Edinburgh Instruments) with a 320 nm laser as the light source. X-ray photoelectron spectroscopy (XPS, PHI Quantera SXM) was performed with Mg Kα radiation and the binding energies were normalized to the C 1s at 284.5 eV. The specific surface areas of the samples were determined by the Microtrac BEL instrument. The photoelectric performance was measured using an electrochemical system (CHI-660B, China). The morphology and microstructure images were obtained by scanning electron microscopy (SEM, FEI QUANTAFEG 250) and transmission electron microscopy (TEM, FEI Talos F200X), respectively.

2.5 Photocatalytic activity evaluation and active species capturing experiments

The photocatalytic activity of the obtained samples was measured by degrading RhB in XPA photoreaction apparatus, 500 W long-arc xenon lamp (the maximum emission at about

470 nm, the light intensity about 150 mW cm^{-2}) with a 420 nm cutoff filter as visible-light source. The temperature of the reaction solution is maintained at approximately 25 °C with continuous cooling. In detail, 25 mg catalyst was dispersed in 50 mL of RhB solution ($c = 1 \times 10^{-5}$ mol L^{-1}) in a quartz tube reactor for ultrasound treating 10 minutes to form a homogeneous suspension solution. Prior to irradiation, the suspension was stirred for 30 minutes away from light, in order to achieve adsorption–desorption equilibrium. Then, the photocatalytic reaction was carried out with a sampling interval of 20 minutes, and the liquid samples were centrifuged at 8000 rpm for 10 minutes and the supernatant analyzed. The absorbance of solution was measured by a spectrophotometer at λ_{max} = 554 nm. The blank test without catalyst was carried out under the same experimental conditions.

To detect the roles of reactive species during the photocatalytic process, the photodegradation performance of RhB has also been tested under the visible-light (λ > 420 nm) irradiation, employing 1.0 mmol L^{-1} edetate disodium (EDTA-2Na), *p*-benzoquinone (BQ) and *tert*-butanol (TBA) as scavengers for holes (h^+), superoxide radicals ($^{\cdot}O_2^-$) and hydroxyl radicals ($^{\cdot}OH$), respectively.

3. Results and discussion

3.1 Characterization

Fig. 1 shows the XRD patterns of the obtained samples. As shown in Fig. 1a and b, h-BN sample shows a main diffraction peak around 26.8°, attributable to the (002) crystal lanes of the graphitic phase h-BN. The diffraction peaks of Bi_2O_3 samples with the main peaks at 2θ = 27.4°, 33.2° and 46.3°, corresponding to the (120), (121) and (041) lattice plane, can be attributed to monoclinic α-Bi_2O_3 (JCPDS No. 41-1449). After post-treatment with ball-milling and sonication, all QS samples featured XRD peaks are similar to those of raw material, but slightly broadened the main peak. As can be seen from Fig. 1c and d, compared with bare Bi_2O_3 QS, the main peaks of h-BN/Bi_2O_3 composites decreased and shifted slightly with increasing the h-BN QS loading, which could indicates the formation of new interface between h-BN QS and Bi_2O_3 QS. On the other hand, the sign of h-BN QS diffraction peak was hardly found in the h-BN/Bi_2O_3 composites, which could be related to its low content and existence mode in the heterostructures.

The SEM images are presented in Fig. 2. As shown in Fig. 2a and b, the plate-like h-BN and h-BN QS are stacked together, with petal-like features observed on the surface. However, compared with raw h-BN, the thickness of h-BN QS become thinner and the size is relatively uniform. For Bi_2O_3 QS (Fig. 2d), the SEM image shows well-dispersed nanoplates, and the morphology is obviously different from that of original bulk Bi_2O_3 (Fig. 2c). After the introduction of h-BN QS, the surface of h-BN/Bi_2O_3 composites (Fig. 2e and f) becomes rough, owing to the layered h-BN QS coating on the surface of the Bi_2O_3 QS. The heterostructure is stacked *via* face-to-face and assembled into a laminated structure to form a large contact interface, which indicates that there is tight contact interface between h-BN QS

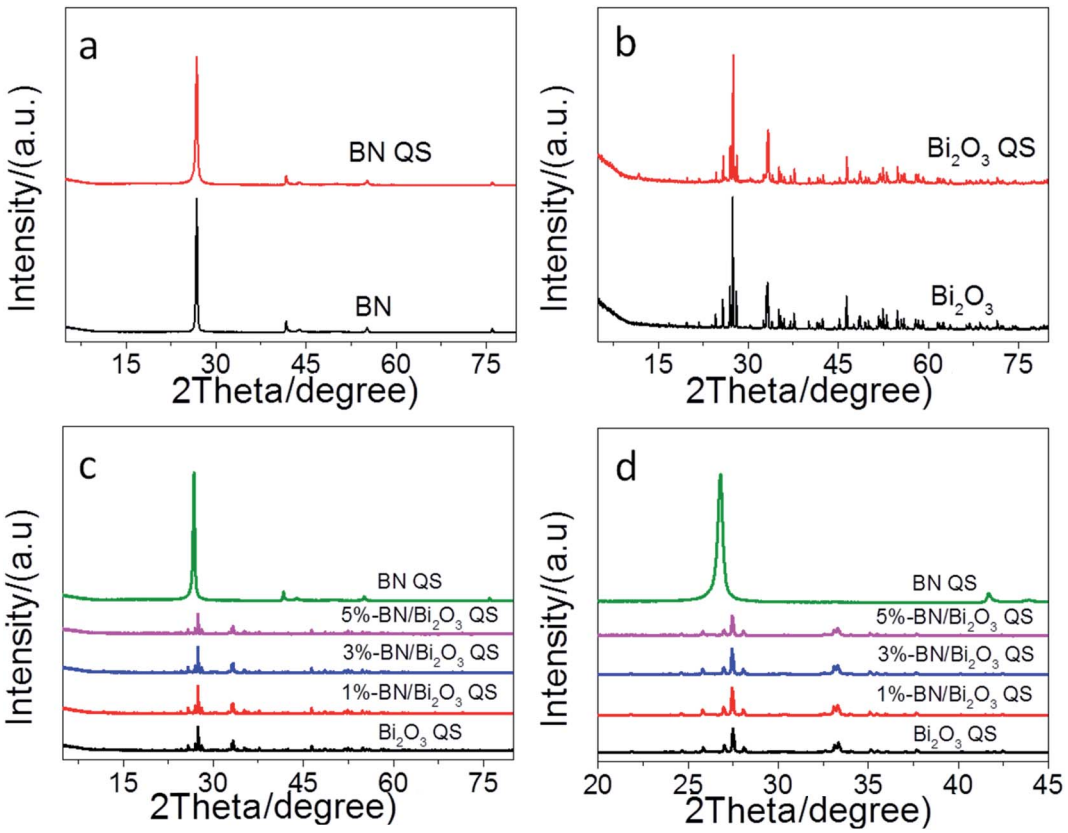

Fig. 1 XRD patterns of (a) BN QS, (b) Bi_2O_3 QS and (c and d) h-BN/Bi_2O_3 composites.

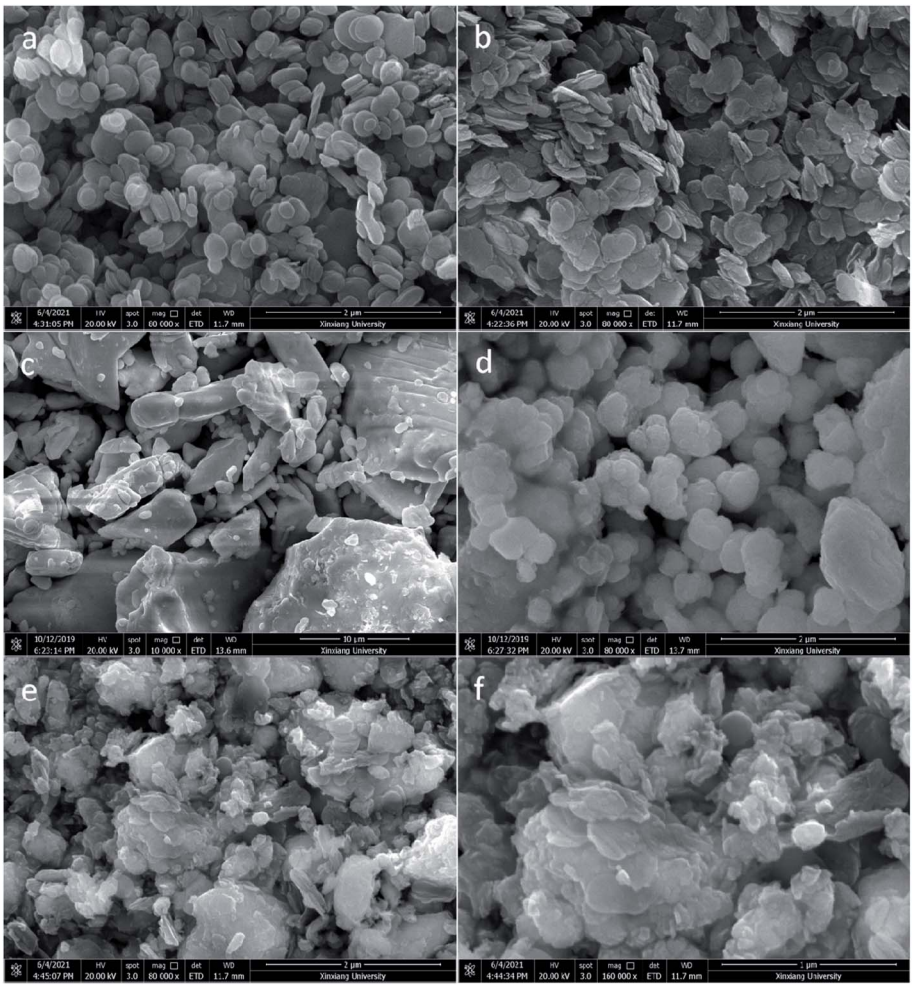

Fig. 2 SEM images of (a) raw h-BN, (b) h-BN QS, (c) raw Bi_2O_3, (d)Bi_2O_3 QS and (e and f) h-BN/Bi_2O_3.

and Bi_2O_3 QS, and potential factors such as defects and local surface structure changes may also play an important role in composites.

The microstructures of samples were further investigated by TEM analysis. In the insets of Fig. 3a and b, the h-BN QS display nanoplate morphology and the Bi_2O_3 QS exhibit uniform and hexagonal nanoplate structure, respectively. Interestingly, as shown in Fig. 3c, the h-BN/Bi_2O_3 composite shows a compact contact interface with an approximate wedge-shaped edges structure. Furthermore, from Fig. 3d and f, the lattice fringe phase with interplanar spacing of 0.290 nm and 0.340 nm are observed in the HRTEM images, which correspond to the crystallographic (211) plane of Bi_2O_3 QS and (002) plane of h-BN QS, respectively. Accordingly, the Bi_2O_3 QS with exposed facets is illustrated in Fig. 3d (in red circles). Given two different lattice fringes were clearly observed from Fig. 3d and f, it is believed that there exists a strong interaction between h-BN QS and Bi_2O_3 QS, implying that the two components form a heterostructure in close contact with each other instead of a simple physical mixture. In Fig. 3g, the EDX spectrum indicates the presence of Bi, O, B, and N elements in the composite. These analysis results also confirmed that h-BN/Bi_2O_3 heterostructure was successfully prepared in the experiment.

The Fourier transform infrared (FT-IR) spectra of h-BN, Bi_2O_3 and h-BN/Bi_2O_3 with different h-BN contents were exhibited in the Fig. 4. For bare Bi_2O_3 QS, the weak and broad band centered at 3500 cm^{-1} is due to stretching vibrations of O–H chemical bond from physically adsorbed water. While the absorption peak at 520 cm^{-1} is attributed to the Bi–O bands of BiO_6 octahedral in Bi_2O_3 structure,[42] the peaks at 1390 cm^{-1} and 803 cm^{-1} are all belonged to the Bi–O bonds stretching vibration.[43] In the IR spectrum of h-BN, there are the intense absorption peaks in the 1380 cm^{-1} and 780 cm^{-1} corresponding to the stretching vibration and deformation vibration of N–B–N bond. In addition, the –OH groups on the surface of h-BN are also contributing to the electron transfer in the photocatalysis.[44] Component structure information corresponding to both h-BN and Bi_2O_3 are presented in the IR spectra of h-BN/Bi_2O_3 composites. Moreover, it is noted that the B–N bond stretching vibration peaks of h-BN/Bi_2O_3 composites display slight shift, implying the strong interaction between the h-BN QS and Bi_2O_3 QS.

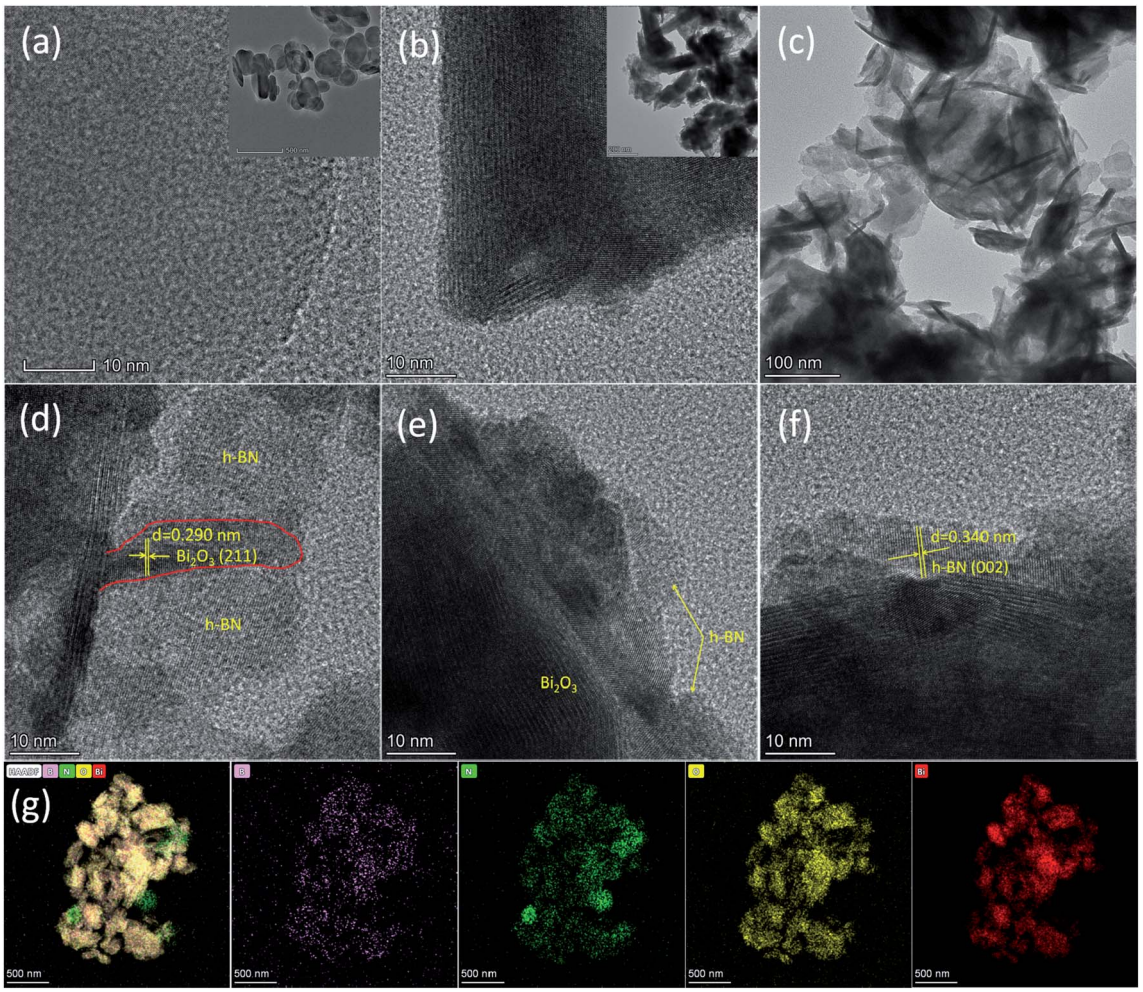

Fig. 3 TEM images of h-BN (a), Bi_2O_3 (b) and h-BN/Bi_2O_3 (c). HRTEM images (d–f) and EDX elemental mapping (g) of h-BN/Bi_2O_3.

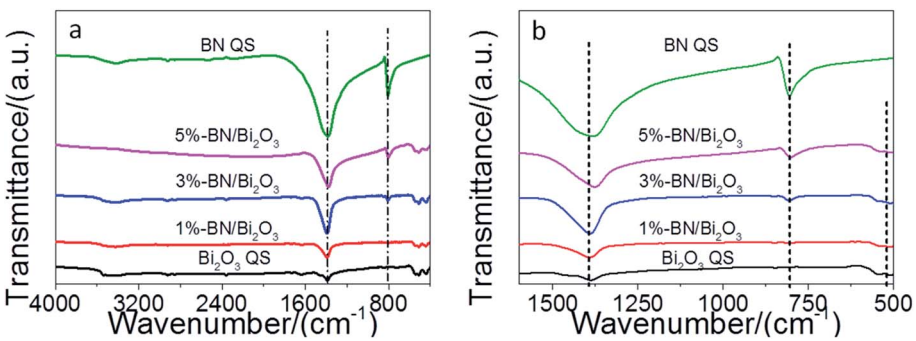

Fig. 4 FT-IR spectra of h-BN QS, Bi_2O_3 QS and h-BN/Bi_2O_3 with different h-BN contents.

In order to explore the effect of h-BN modification on the light absorption of Bi_2O_3, the ultraviolet-visible optical absorption spectra of the samples in the wavelength range of 230–800 nm were displayed in Fig. 5. It is found that the absorption edge of h-BN/Bi_2O_3 samples changes slightly with the increase of h-BN content, enhancing the visible-light absorption at the wavelength below 420 nm, which is attributed to the narrowing of the band gap of the composites with the h-BN introduced to the Bi_2O_3. Compared with bare Bi_2O_3, the slight wider absorption edge and the narrower band gap indicate that h-BN/Bi_2O_3 has greater carrier concentration, which can be conducive to photocatalytic reactions.

The elements and surface states of the obtained samples were acquired to further confirm by X-ray photoelectron spectroscopy (XPS) characterization. The binding energy (BE) of the measured elements was corrected according to C 1s (284.5 eV).

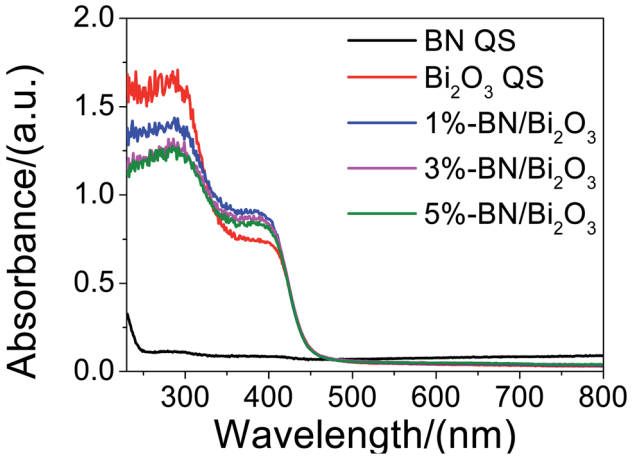

Fig. 5 The UV-vis absorption spectra for the obtained samples.

As expected, the survey scan XPS spectrum (Fig. 6a) showed that all chemical elements of B, N, Bi and O in h-BN/Bi_2O_3 composite were detected. As shown from the high-resolution spectrum of Bi 4f (Fig. 6b), the BEs of 159.2 eV (Bi $4f_{7/2}$) and 164.5 (Bi $4f_{5/2}$) are attributed to Bi^{3+}. Similarly, the peak value at 530.1 eV in Fig. 6c can be designated as O 1s and is characteristic of Bi–O binding energy in Bi_2O_3. As can be seen from Fig. 6d and e, the signals of B 1s and N 1s indicated the existence of BN in h-BN/Bi_2O_3 composite. Meanwhile, compared with bare h-BN QS, the BEs of B and N core electrons of h-BN/Bi_2O_3 displays a positive shift ~0.2 eV, suggesting the migration of photogenerated carriers in the interface of h-BN/Bi_2O_3 heterostructure. These XPS results demonstrate that the structure of h-BN/Bi_2O_3 is a hybrid structure with strong interaction between two components interface, and this interaction is beneficial for enhancing the photocatalytic performance. XPS analysis confirms the coexistence of h-BN and Bi_2O_3 in h-BN/Bi_2O_3 sample and further demonstrating h-BN/Bi_2O_3 heterostructure has been successfully prepared by liquid phase self-assembly method. Further, comparing the peaks located at h-BN QS, Bi_2O_3 QS and h-BN/Bi_2O_3 indicate that the BE of B 1s, N 1s and Bi 4f both increased 0.2 eV, 0.2 eV and 0.1 eV, respectively, except for the peak of O 1s spectrum. This higher binding energy indicated that more h^+ were concentrated on the h-BN surface *via* contact with Bi_2O_3. In contrast to Bi_2O_3 BE, a slight increase was indicated in Bi 4f spectra for 0.1 eV. This suggests that the electron density around the element and defect in Bi_2O_3 was a decrease caused by the pile with h-BN.[45] These increases in BEs corresponding to electrons transferred from Bi_2O_3 to h-BN might be generated by the internal electron field at the interface between Bi_2O_3 and h-BN.[46] All the above results suggested that the Schottky heterojunction was formed between Bi_2O_3 QS and h-BN QS by strong interaction rather than the simple physical mixture.

The specific surface areas of Bi_2O_3 QS, h-BN QS and h-BN/Bi_2O_3 composite were characterized by nitrogen adsorption–desorption isotherms in the Fig. 7. The BET surface areas of raw Bi_2O_3, Bi_2O_3 QS, raw h-BN, h-BN QS and 3wt%-BN/Bi_2O_3 were measured to be 0.14 $m^2 g^{-1}$, 9.79 $m^2 g^{-1}$, 12.93 $m^2 g^{-1}$, 41.33 $m^2 g^{-1}$ and 12.53 $m^2 g^{-1}$, respectively. From the BET data, the surface area of the 3wt%-BN/Bi_2O_3 sample is about 1.3 times as large as Bi_2O_3 QS, suggesting that the enlarged surface area can provide more active sites for photocatalytic reaction. It is generally believed that the adsorption performance of a photocatalyst towards the target pollutant is one of the main factors to affect the reaction kinetics. Therefore, it is considered that the surface area of h-BN/Bi_2O_3 may be an important index affecting the catalytic efficiency. As can be seen from the pore size distribution curves (inset), it reflects the effect of h-BN QS on the pore size and volume of heterostructures. It is well known that higher specific surface area can provide rich active reaction sites and promote the adsorption of more pollutant molecules on its surface. Moreover, it can be seen from the insertion pore size distribution diagram that the catalyst is rich in mesopores. The presence of large mesopores in a porous photocatalyst favors multilight scattering/reflection, resulting in enhanced harvesting of the exciting light and thus improved photocatalytic activity.[47,48] In addition, large mesopores facilitate mass transport, resulting in improved performance.[49,50] Therefore, the h-BN/Bi_2O_3 is expected to possess a better photocatalytic activity than Bi_2O_3.

Electron paramagnetic resonance (EPR) spectroscopy can provide information about the valence state, concentration, local environment and interaction properties of transition metal ions. Moreover, the EPR spectrum can provide more evidence for the existence of defect states in the crystal structure and unpaired electrons in materials. In Fig. 8a, the stronger signal strength indicates of raw h-BN that the characteristic peak of defect, which is caused by the occupation and absorption of rich electrons at the defect site by adsorbed oxygen molecules. During the process of preparation quantum sheets by ball milling, the crystal lattices of sample undergo severe crystal lattice dislocations, plastic deformation, producing stresses and strains. Thus a large number of stripping- and point-defects are produced. On the contrary, the Bi_2O_3 QS uniquely exhibits a symmetrical EPR signal, manifesting the electron trapping at oxygen vacancies in the Fig. 8b, it shows that the corresponding Bi_2O_3 QS has a large number of oxygen vacancy defects, further validated by the obviously observed lattice disorder in Fig. 3. On the contrary, the defects of h-BN mainly exist in raw bulk materials. As can be seen from the EPR signal of h-BN/Bi_2O_3 composite is extremely weak in Fig. 8c and d. Based on EPR analysis, it is speculated that oxygen vacancies mainly exist on the surface of Bi_2O_3 QS, h-BN/Bi_2O_3 mainly presents face-to-face stacking layered structure. These analysis results also confirmed the formation of a hybrid heterostructure in the contact interface between Bi_2O_3 and h-BN, which can greatly promote the separation of photogenerated e^-–h^+ pairs.

Photoluminescence (PL) spectra were used to explore the transfer and separation efficiency of carriers. The effective separation of photogenerated e^-–h^+ pairs is the key role in the photocatalytic process. The PL spectra of the Bi_2O_3 QS and BN/Bi_2O_3 were shown in Fig. 9a. The Bi_2O_3 QS sample displayed the emission peak centered at around 468 nm under the excitation wavelength of 320 nm. The PL intensity of the BN QS modified

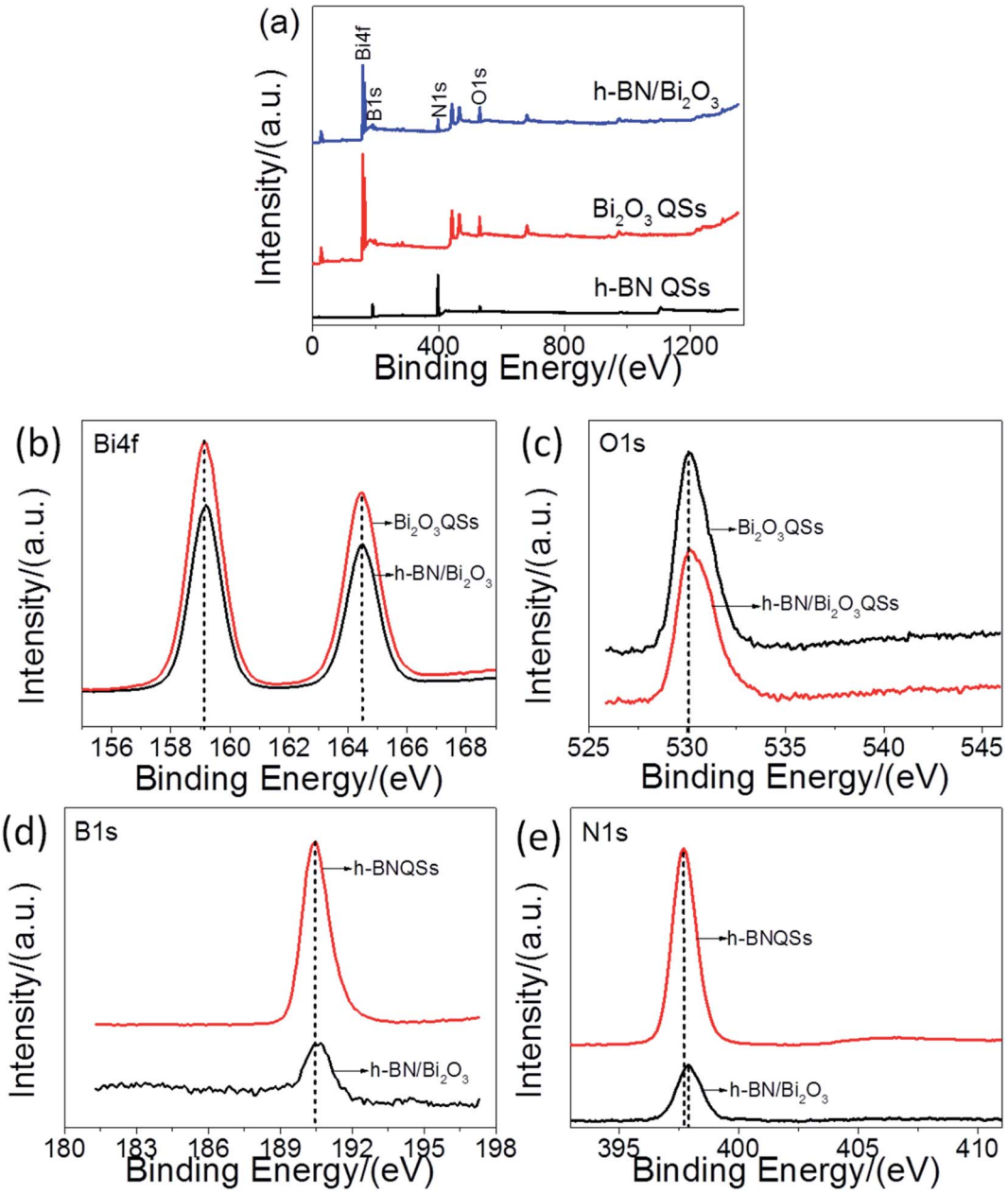

Fig. 6 (a) XPS survey spectra, high-resolution XPS spectra of (b) Bi 4f, (c) O 1s, (d) B 1s, and (e) N 1s for Bi_2O_3 QS, h-BN QS and the 3%-BN/Bi_2O_3 composite.

Bi_2O_3 QS become weaker than that of the pure Bi_2O_3 QS, implying the presence of h-BN QS in this system could decrease the recombination rate of photogenerated e^-–h^+ pairs. In addition, lower PL spectra quenching occurs on the 3%-BN/Bi_2O_3 sample relative to Bi_2O_3 QS, suggesting the suppressed carriers recombination and improved carriers separation efficiency, possibly owning to the formation of h-BN/Bi_2O_3 heterostructure with strong interaction.

Moreover, time-resolved photoluminescence (TRPL) spectroscopy was employed to further explore the photo-excited carrier dynamics. As shown in Fig. 9b, the average fluorescence lifetime of 3%-BN/Bi_2O_3 composite is calculated to be 2.36 ns, which is longer than that of Bi_2O_3 (1.66 ns), indicating the prolonged lifetime of photogenerated carriers in the composite due to the presence of the Schottky heterojunction, which prevent the recombination of photogenerated e^-–h^+ pairs in Bi_2O_3. Thus, it is that the 3%-BN/Bi_2O_3 has both longer fast decay lifetime (τ_1) and slow decay lifetime (τ_2) than that Bi_2O_3 QS (inset in Fig. 7b).

It is well known that photocurrent comes from the diffusion of photoelectrons to the back contact. In order to investigate the transition of photogenerated electrons before and after h-BN modification, photoelectrochemical measurement was performed. Fig. 10 displays the photocurrent response of h-BN/

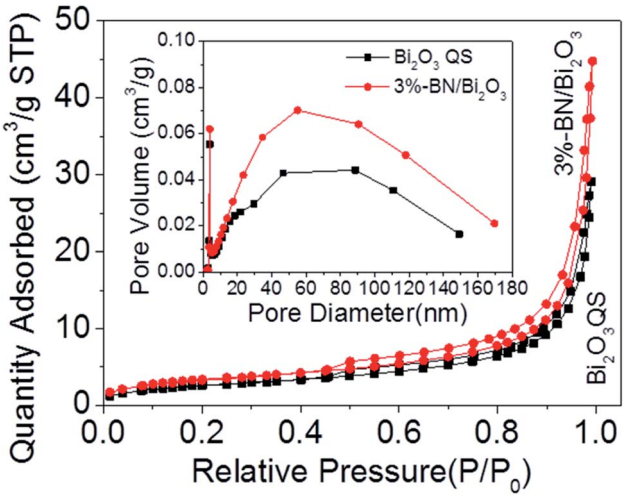

Fig. 7 N_2 sorption isotherms and corresponding pore size distribution curves (inset) of samples.

Bi_2O_3 and Bi_2O_3 under visible-light irradiation. It can be observed that the 3%-BN/Bi_2O_3 shows remarkably increased photocurrent intensity than 5%-BN/Bi_2O_3 and the single component Bi_2O_3, implying that photogenerated carrier separation efficiency is enhanced and more photoexcited carriers are generated. This result is consistent with the catalytic activity.

The photocatalytic activities of the as-prepared samples were evaluated by photocatalytic degradation RhB solution under visible-light irradiation and the concentration changes are provided in Fig. 11. As shown in Fig. 11a, the blank test demonstrated that RhB was stable under visible-light irradiation for 120 minutes. The results showed that the raw Bi_2O_3 exhibited very poor photocatalytic activity, with only 5% RhB degradation, after visible-light irradiation for 120 minutes. In comparison with bare Bi_2O_3 QS, the h-BN/Bi_2O_3 composites exhibit superior photocatalytic activities and the h-BN QS content plays a key role. The experimental results show that RhB ($c = 1 \times 10^{-5}$ mol L^{-1}) can be completely degraded by 3%-BN/Bi_2O_3 catalyst within 120 minutes under visible-light irradiation, while the sole Bi_2O_3 QS can only decompose 60% of RhB during the same interval. With the content of h-BN increasing, it leads to the decrease of photocatalytic activity. This was attributed to that while a massive overdose of h-BN covered on the surface of Bi_2O_3 would shield light absorb and the reaction active sites. Meanwhile, the kinetic properties of photocatalytic reaction were further studied. The degradation reaction rate is subject to the pseudo-first order kinetic equation ($-\ln(C/C_0) = kt$), there is a nice linear correlation for the experimental data. As shown in Fig. 11b, 3%-BN/Bi_2O_3 sample has the best photocatalytic activity, which rate constant value (k = 0.03191 min^{-1}) is about 4.5 times that of Bi_2O_3 QS (k = 0.00702 min^{-1}). The enhancement of photocatalytic activity of

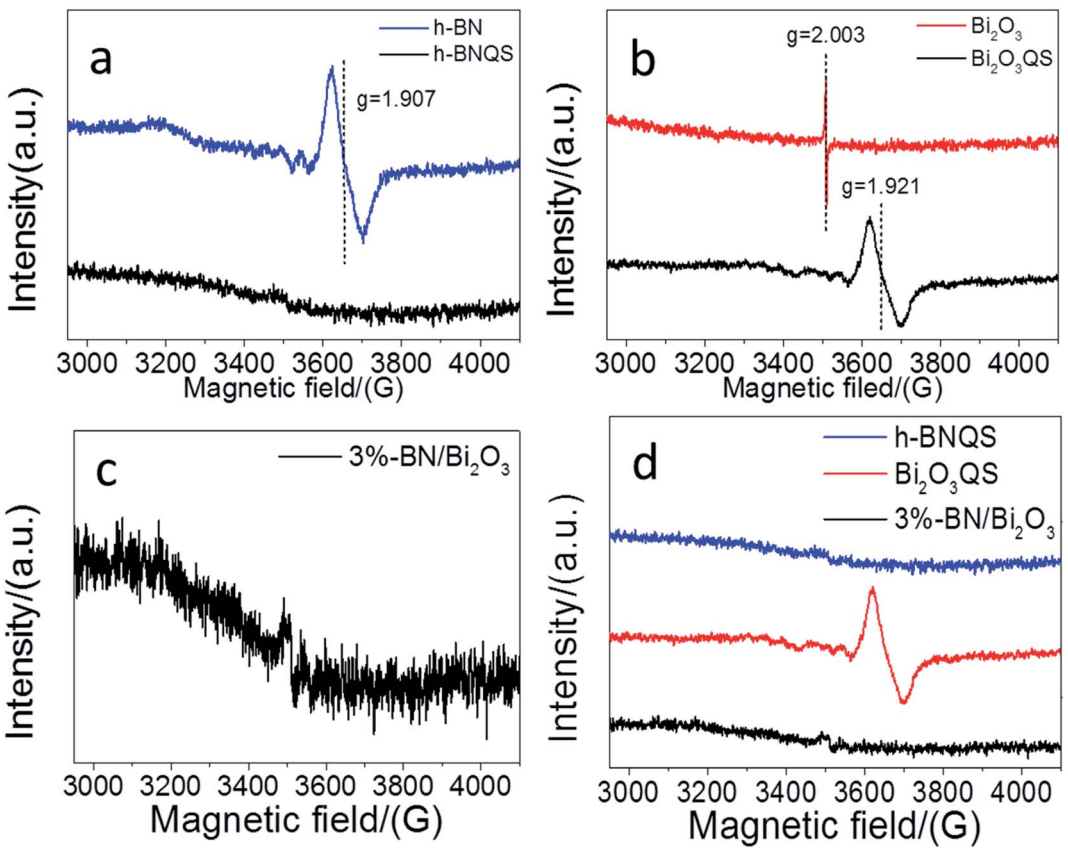

Fig. 8 The electron paramagnetic resonance spectra of (a) h-BN, (b) Bi_2O_3 and (c and d) h-BN/Bi_2O_3.

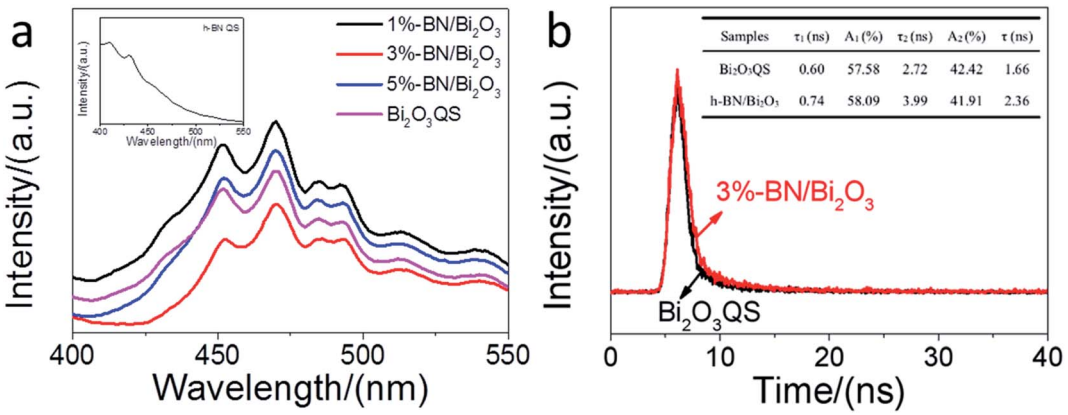

Fig. 9 (a) PL spectra of Bi_2O_3 QS and BN/Bi_2O_3 composites (inset of the h-BN QS), (b) time-resolved photoluminescence decay spectra of Bi_2O_3 QS and 3wt%-BN/Bi_2O_3.

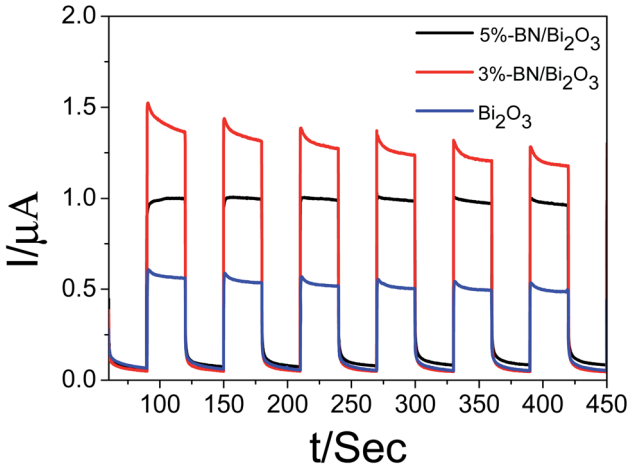

Fig. 10 Transient photocurrent responses of Bi_2O_3 and h-BN/Bi_2O_3 under visible-light irradiation.

h-BN/Bi_2O_3 may also be due to energy band well matching in the heterostructure.

In order to understanding the catalysis mechanism, the reactive species of photocatalysis are very important. As shown in Fig. 12a, the photocatalytic activity of h-BN/Bi_2O_3 was inhibited by EDTA-2Na and TBA, and to a lesser extent by BQ, indicating the significant roles of h^+ and $^{\bullet}OH$ and suggesting a minor role of $^{\bullet}O_2^-$ radical in the degradation process. It should be noted that the influence of $^{\bullet}O_2^-$ radical on the photocatalytic activity of h-BN/Bi_2O_3 is less significant than that of Bi_2O_3/g-C_3N_4,[51] which shows the overall influence on the two components of the composite. In h-BN/Bi_2O_3 photocatalytic system, the oxidizing h^+ and $^{\bullet}OH$ radicals worked as the main active groups, contributed to the photocatalytic oxidation ability.

In addition to photocatalytic activity, the durability of catalyst is also very important for its practical application. The stability of the obtained h-BN/Bi_2O_3 photocatalyst was also evaluated *via* the circulating run experiment of RhB degradation. As shown in Fig. 12b, the crystal structure of h-BN/Bi_2O_3 catalyst remains unchanged and there is no photo corrosion after 3 cycling runs in 6 h, and its photocatalytic performance did not show a distinct attenuation, which indicate that the h-BN/Bi_2O_3 catalysts possess good reusability for practical applications.

As a binary h-BN/Bi_2O_3 composite with the characteristics of Schottky heterojunction, it shows excellent catalytic properties under visible-light irradiation. A solid-state Schottky junction mechanism can be proposed to explain the effective

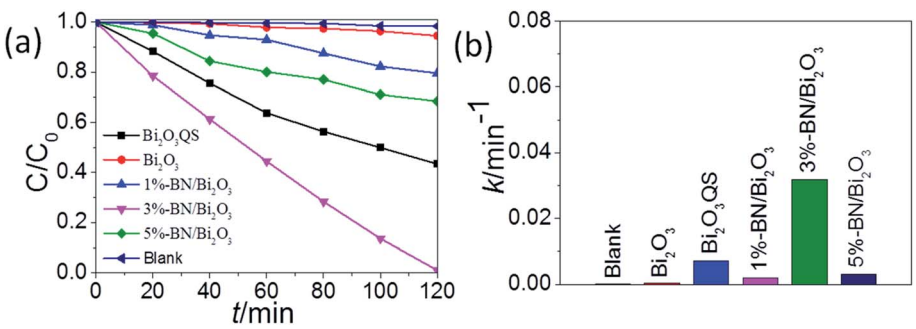

Fig. 11 (a) Variation curve of RhB concentration with irradiation time. (b) The first-order kinetics of photocatalytic reaction under visible-light irradiation (λ > 420 nm).

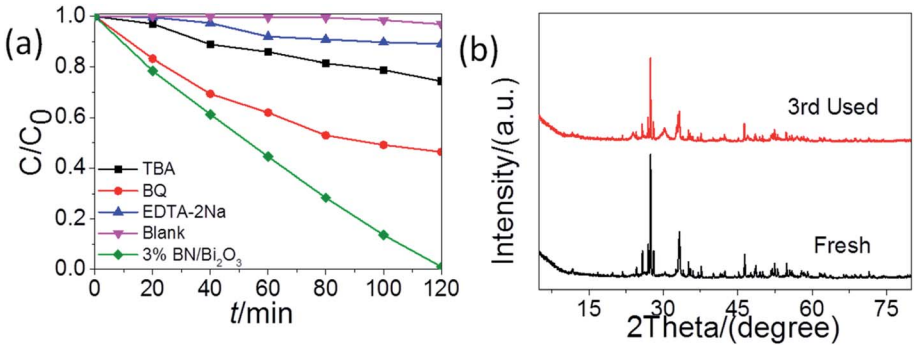

Fig. 12 (a) Effects of reactive species scavengers on photocatalytic performance of BN/Bi_2O_3. (b) Cycling runs of BN/Bi_2O_3 under visible-light irradiation (λ > 420 nm).

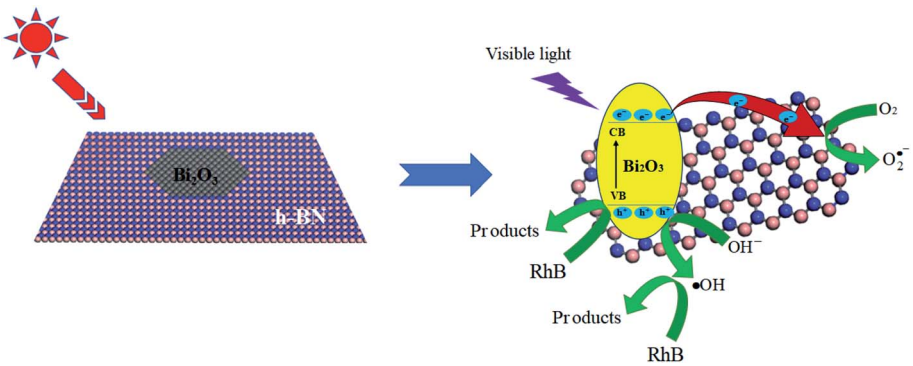

Fig. 13 The proposed photocatalytic mechanism of h-BN/Bi_2O_3 under visible-light irradiation.

photocatalytic response of h-BN/Bi_2O_3. Under the light excitation, the interface can react with electrons as an intermediate, and indirectly lead to the transmission of electrons. Regarding the activity enhancing mechanism through the incorporation of h-BN QS and Bi_2O_3 QS nanostructures, the photocatalytic mechanism of h-BN/Bi_2O_3 is tentatively proposed and schematically illustrated in Fig. 13. In h-BN/Bi_2O_3 systems, the h-BN QS could be the photogenerated carrier transfer and separation promoter. Under visible light irradiation, Bi_2O_3 can be easily excited to yield photon-generated carriers, that is, photoinduced electrons from the valence band are easily transferred to the corresponding conduction band, leaving h^+ in the valence band of Bi_2O_3. The h^+ on the VB of Bi_2O_3 (2.69 eV *vs.* NHE) is capable to generate $^{\bullet}OH$ ($E^0_{^{\bullet}OH/OH^-} = 1.99$ eV *vs.* NHE), while the CB of Bi_2O_3 barely meets the requirement for O_2 reduction ($E^0_{O_2/^{\bullet}O_2^-} = -0.046$ eV *vs.* NHE), suggesting that $^{\bullet}O_2^-$ can be generated in this system. The light excitation electrons generated form Bi_2O_3 transfer to h-BN, while photogenerated holes on h-BN transfer to Bi_2O_3, enhancing the e^-–h^+ pairs effective separation *via* the heterojunction interface. Therefore, the photogenerated carriers are spatially separated and their lifetime can be significant improved for h-BN/Bi_2O_3 composites which bring about superior photocatalytic activity and stability. According to the above mentioned process, the efficient photocatalytic degradation progress of RhB can smoothly proceed.

The possible processes can be described as follows:

$$Bi_2O_3 + h\nu \rightarrow Bi_2O_3\,(h^+ + e^-) \quad (1)$$

$$Bi_2O_3\,(h^+ + e^-) + BN \rightarrow Bi_2O_3\,(h^+) + BN\,(e^-) \quad (2)$$

$$BN\,(e^-) + O_2 \rightarrow BN + {}^{\bullet}O_2^- \quad (3)$$

$${}^{\bullet}O_2^- + H_2O \rightarrow HO_2^{\bullet} + OH^- \quad (4)$$

$$HO_2^{\bullet} + H_2O \rightarrow H_2O_2 + {}^{\bullet}OH \quad (5)$$

$$H_2O_2 + h\nu \rightarrow 2{}^{\bullet}OH \quad (6)$$

$$h^+ + {}^{\bullet}OH + RhB \rightarrow \text{Intermediate} \rightarrow CO_2 + H_2O \quad (7)$$

This enhanced photocatalytic performance of h-BN/Bi_2O_3 heterostructure is attributed to the increased efficiency of photoinduced generated carries transfer, suppressed photogenerated e^-–h^+ recombination probability and produced more active species with the introduction of h-BN QS in the Bi_2O_3 QS semiconductor.

4. Conclusions

Herein, a facile method of fabricating h-BN/Bi_2O_3 heterostructure from Bi_2O_3 QS and h-BN QS is reported. Quantum sheet has both novel bulk characteristics and two-dimensional characteristics, resulting in abundant unique phenomena.

Creating 2D geometry quantum sheets from the raw bulk h-BN and Bi_2O_3 can significantly advance the high-performance photocatalysts design, which can induce high surface chemical activity, rapid interfacial charge transfer and promote the adsorption of reactants, so as to improve the photocatalytic performance. 2D h-BN/Bi_2O_3 heterostructure self-assembled by the surface stacking of Bi_2O_3 QS and h-BN QS has intimate interface with strong interaction, which is conducive to charge transfer and separation in the photocatalytic process. In addition, potential factors such as surface defects and local surface structure changes may also play an important role in the heterostructure. These experimental facts show that the advantages of h-BN/Bi_2O_3 composite composed of QSs exhibit significant photocatalytic activity, which is expected to become a promising alternative for wastewater purification.

Author contributions

Zhou Jianwei: conceptualization, data curation, formal analysis, writing – original draft. Duo Fangfang: writing – review & editing. Wang Chubei: investigation, writing – review & editing. Chu Liangliang: investigation, writing – review & editing. Zhang Mingliang: writing – review & editing. Yan Donglei: writing – review & editing.

Conflicts of interest

The authors declare no conflict of interest.

Acknowledgements

This work is supported by the Project of Science and Technology of the Henan Province (192102310496).

References

1 X. Li, J. Yu, S. Wageh, A. A. Al-Ghamdi and J. Xie, Graphene in photocatalysis: a review, *Small*, 2016, **12**, 6640–6696.
2 X. J. Chen, Q. Chen, W. J. Jiang, Z. Wei and Y. F. Zhu, Separation-free TiO_2-graphene hydrogel with 3D network structure for efficient photoelectrocatalytic mineralization, *Appl. Catal., B*, 2017, **211**, 106–113.
3 C. Lai, M. M. Wang, G. M. Zeng, Y. G. Liu, D. L. Huang, C. Zhang, R. Z. Wang, P. Xu, M. Cheng and C. Huang, Synthesis of surface molecular imprinted TiO_2/graphene photocatalyst and its highly efficient photocatalytic degradation of target pollutant under visible light irradiation, *Appl. Surf. Sci.*, 2016, **390**, 368–376.
4 Q. Zheng, D. P. Durkin, J. E. Elenewski, Y. Sun, N. A. Banek, L. Hua, H. Chen, M. J. Wagner, W. Zhang and D. Shuai, Visible-light-responsive graphitic carbon nitride: Rational design and photocatalytic applications for water treatment, *Environ. Sci. Technol.*, 2016, **50**, 12938–12948.
5 F. T. Yi, J. Q. Ma, C. W. Lin, H. N. Zhang, Y. X. Qian, H. X. Jin and K. F. Zhang, Electronic and thermal transfer actuating memory catalysis for organic removal by a plasmonic photocatalyst, *Chem. Eng. J.*, 2022, **427**, 132028–132038.
6 F. T. Yi, H. H. Gan, H. F. Jin, W. Y. Zhao, K. F. Zhang, H. X. Jin, H. N. Zhang, Y. X. Qian and J. Q. Ma, Sulfur- and chlorine-co-doped g-C_3N_4 nanosheets with enhanced active species generation for boosting visible-light photodegradation activity, *Sep. Purif. Technol.*, 2020, **233**, 115997–116009.
7 Q. J. Xiang, J. G. Yu and M. Jaroniec, Graphene-based semiconductor photocatalysts, *Chem. Soc. Rev.*, 2012, **41**, 782–796.
8 G. F. Liao, C. X. Li, X. Z. Li and B. Z. Fang, Emerging polymeric carbon nitride Z-scheme systems for photocatalysis, *Cell Rep. Phys. Sci.*, 2021, **2**, 100355–100390.
9 G. F. Liao, C. X. Li, B. Z. Fang and H. M. Yang, Emerging frontiers of Z-schemephotocatalytic systems, *Trends Chem.*, 2022, **4**(2), 111–127.
10 H. M. Gao, D. Y. Zhang, M. N. Yang and S. Dong, Photocatalytic behavior of fluorinated rutile TiO_2 (110) surface: Understanding from the band model, *Sol. RRL*, 2017, **1**, 1700183–1700188.
11 T. Hisatomi, J. Kubota and K. Domen, Recent advances in semiconductors for photocatalytic and photoelectrochemical water splitting, *Chem. Soc. Rev.*, 2014, **43**, 7520–7536.
12 C. Y. Zhou, C. Lai, C. Zhang, G. M. Zeng, D. L. Huang, M. Cheng, L. Hu, W. P. Xiong, M. Chen, J. J. Wang, Y. Yang and L. B. Jiang, Semiconductor/boron nitride composites: Synthesis, properties, and photocatalysis applications, *Appl. Catal., B*, 2018, **238**, 6–18.
13 X. Li, J. Zhang, S. J. Zhang, S. S. Xu, X. G. Wu, J. C. Chang and Z. L. He, Hexagonal boron nitride composite photocatalysts for hydrogen production, *J. Alloys Compd.*, 2020, **864**, 158153–158191.
14 K. L. Zhang, Y. L. Feng, F. Wang, Z. C. Yang and J. Wang, Two dimensional hexagonal boron nitride (2D-hBN): synthesis, properties and applications, *J. Mater. Chem. C*, 2017, **5**, 11992–12022.
15 Q. Weng, X. Wang, X. Wang, Y. Bando and D. Golberg, Functionalized hexagonal boron nitride nanomaterials: emerging properties and applications, *Chem. Soc. Rev.*, 2016, **45**, 3989–4012.
16 Z. He, C. Kim, L. Lin, T. H. Jeon, S. Lin, X. Wang and W. Choi, Formation of heterostructures *via* direct growth CN on h-BN porous nanosheets for metal-free photocatalysis, *Nano Energy*, 2017, **42**, 58–68.
17 Z. G. Chen, X. L. Chen, J. Di, Y. L. Liu, S. Yin, J. X. Xia and H. M. Li, Graphene-like boron nitride modified bismuth phosphate materials for boosting photocatalytic degradation of enrofloxacin, *J. Colloid Interface Sci.*, 2017, **492**, 51–60.
18 C. S. Zhu, J. T. Zheng, L. Y. Fang, P. Hu, Y. K. Liu, X. Q. Cao and M. B. Wu, Advanced visible-light driven photocatalyst with enhanced chargeseparation fabricated by facile deposition of Ag_3PO_4 nanoparticles on graphene-like h-BN nanosheets, *J. Mol. Catal. A: Chem.*, 2016, **424**, 135–144.
19 Q. H. Weng, Y. Ide, X. B. Wang, X. Wang, C. Zhang, X. F. Jiang, Y. M. Xue, P. C. Dai, K. Komaguchi, Y. Bando and D. Golberg, Design of BN poroussheets with richly

exposed (002) plane edges and their application as TiO_2 visible light sensitizer, *Nano Energy*, 2015, **16**, 19–27.

20 S. S. Ding, D. J. Mao, S. G. Yang, F. Wang, L. J. Meng, M. S. Han, H. He, C. Sun and B. Xu, Graphene-analogue h-BN coupled Bi-rich $Bi_4O_5Br_2$ layered microspheres for enhanced visible-light photocatalytic activity and mechanism insight, *Appl. Catal., B*, 2017, **210**, 386–399.

21 S. Raheman, R. S. Mane, H. M. Wilson and N. Jha, CdSe quantum dot/white graphene hexagonal porous boron nitride sheet (h-PBNs) heterostructure photocatalyst for solar driven H_2 production, *J. Mater. Chem. C*, 2021, **9**, 9331–9338.

22 D. Tu, H. W. Liao and Q. L. Deng, Synthesis of BN/g-C_3N_4 as visible-light-driven photocatalysts for degradation of different organic pollutants, *ChemistrySelect*, 2018, **3**, 7170–7177.

23 N. Wang, G. Yang, H. X. Wang, R. Sun and C. P. Wong, Visible light-responsive photocatalytic activity of boron nitride incorporated composites, *Front. Chem.*, 2018, **6**, 440–452.

24 J. K. Ren and P. Innocenzi, 2D Boron nitride heterostructures: Recent advances and future challenges, *Small Struct.*, 2021, **8**, 2100068–2100083.

25 C. J. Huang, C. Chen, M. W. Zhang, L. H. Lin, X. X. Ye, S. Lin, M. Antonietti and X. C. Wang, Carbon-doped BN nanosheets for metal-free photoredox catalysis, *Nat. Commun.*, 2015, **6**, 7698–7704.

26 Y. H. Cao, R. Y. Zhang, T. L. Zhou, S. M. Jin, J. D. Huang, L. Q. Ye, Z. Huang, F. Wang and Y. Zhou, B-O bond in ultrathin boron nitride nanosheets to promote photocatalytic carbon dioxide conversion, *ACS Appl. Mater. Interfaces*, 2020, **12**, 9935–9950.

27 D. Deng, K. S. Novoselov, Q. Fu, N. Zheng, Z. Tiang and X. Bao, Catalysis with two-dimensional materials and their heterostructures, *Nat. Nanotechnol.*, 2016, **11**, 218–230.

28 X. Wang, G. Sun, N. Li and P. Chen, Quantum dots derived from two-dimensional materials and their applications for catalysis and energy, *Chem. Soc. Rev.*, 2016, **45**, 2239–2262.

29 C. Han, Y. Zhang, P. Gao, S. Chen, X. Liu, Y. Mi, J. Zhang, Y. Ma, W. Jiang and J. Chang, High-yield production of MoS_2 and WS_2 quantum sheets from their bulk materials, *Nano Lett.*, 2017, **17**, 7767–7772.

30 J. T. Yuan, W. B. Chen and J. Lou, Two dimensional heterostructure: perfect platform for exploring interface interaction, *Sci. Bull.*, 2017, **62**, 381–382.

31 Y. Z. Wang, Z. Y. Zhang, Y. C. Mao and X. D. Wang, Two-dimensional non-layered materials for electrocatalysis, *Energy Environ. Sci.*, 2020, **13**, 3993–4016.

32 G. Bandoli, D. Barreca, E. Brescacin, G. A. Rizzi and E. Tondello, Pure and mixed phase Bi_2O_3 thin films obtained by metal organic chemical vapor deposition, *Chem. Vap. Deposition*, 1996, **2**, 238–241.

33 Y. C. Wu, Z. M. Liu, Y. R. Li, J. T. Chen, X. X. Zhu and P. Na, Construction of 2D-2D TiO_2 nanosheet/layered WS_2 heterojunctions with enhanced visible-light-responsive photocatalytic activity, *Chin. J. Catal.*, 2019, **40**, 60–69.

34 Q. L. Xu, B. C. Zhu, C. J. Jiang, C. Bei and J. Yu, Constructing 2D/2D Fe_2O_3/g-C_3N_4 direct Z-scheme photocatalysts with enhanced H_2 generation performance, *Sol. RRL*, 2018, **2**, 1800006–1800016.

35 W. H. He, Y. W. Wang, C. M. Fan, Y. Wang, X. Zhang, J. Liu and R. Li, Enhanced charge separation and increased oxygen vacancies of h-BN/OV-BiOCl for improved visible light photocatalytic performance, *RSC Adv.*, 2019, **9**, 14286–14295.

36 Z. Y. Zhang, J. D. Huang and M. Y. Zhang, Ultrathin hexagonal SnS_2 nanosheets coupled with g-C_3N_4 nanosheets as 2D/2D heterojunction photocatalysts toward high photocatalytic activity, *Appl. Catal., B*, 2015, **163**, 298–305.

37 F. K. Meng, J. T. Li, S. K. Cushing, M. J. Zhi and N. Q. Wu, Solar hydrogen generation by nanoscale p-n junction of p-type molybdenum disulfide/n-type nitrogen-doped reduced graphene oxide, *J. Am. Chem. Soc.*, 2013, **135**, 10286–10289.

38 X. Q. An, J. C. Yu and J. W. Tang, Biomolecule-assisted fabrication of copper doped SnS_2 nanosheet-reduced graphene oxide junctions with enhanced visible-light photocatalytic activity, *J. Mater. Chem. A*, 2014, **2**, 1000–1005.

39 J. Li, G. M. Zhan, Y. Yu and L. Zhang, Superior visible light hydrogen evolution of Janus bilayer junctions *via* atomic level charge flow steering, *Nat. Commun.*, 2016, **7**, 1–9.

40 Z. Xing, J. Hu, M. Ma, H. Lin, Y. M. An, Z. H. Liu, Y. Zhang, J. Y. Li and S. H. Yang, From one to two: In-situ construction of an ultrathin 2D-2D closely-bonded heterojunction from a single-phase monolayer nanosheet, *J. Am. Chem. Soc.*, 2019, **141**, 19715–19727.

41 X. L. Yang, F. F. Qian, G. J. Zou, M. L. Li, J. R. Lu, Yi M. Li and M. T. Bao, Facile fabrication of acidified g-C_3N_4/g-C_3N_4 hybrids with enhanced photocatalysis performance under visible light irradiation, *Appl. Catal., B*, 2016, **193**, 22–35.

42 V. Dimitrov, Y. Dimitriev and A. Montenero, IR spectra and structure of V_2O_5-GeO_2-Bi_2O_3 glasses, *J. Non-Cryst. Solids*, 1994, **180**, 51–57.

43 L. Liu, J. Jiang, S. Jin, Z. Xia and M. Tang, Hydrothermal synthesis of β-bismuth oxide nanowires from particles, *CrystEngComm*, 2011, **13**, 2529–2532.

44 D. J. Lee, B. Lee, K. H. Park, H. J. Ryu, S. Jeon and S. H. Hong, Scalable exfoliation process for highly soluble boron nitride nanoplatelets by hydroxide-assisted ball milling, *Nano Lett.*, 2015, **15**, 1238–1244.

45 F. T. Yi, J. Q. Ma, C. W. Lin, L. Y. Wang, H. N. Zhang, Y. X. Qian and K. F. Zhang, Insights into the enhanced adsorption/photocatalysis mechanism of a $Bi_4O_5Br_2$/g-C_3N_4 nanosheet, *J. Alloys Compd.*, 2020, **821**, 153557–153569.

46 F. T. Yi, J. Liu, G. P. Liang, X. Xiao and H. F. Wang, Insight into the enhanced degradation mechanism of g-C_3N_4/g-C_3N_5 heterostructures through photocatalytic molecular oxygen activation in Van der Waals junction and excitation, *J. Alloys Compd.*, 2022, **905**, 164064–164076.

47 B. Z. Fang, A. Bonakdarpour, K. Reilly, Y. L. Xing, F. Taghipour and D. P. Wilkinson, Large-scale synthesis of TiO_2 microspheres with hierarchical nanostructure for highly efficient photodriven reduction of CO_2 to CH_4, *ACS Appl. Mater. Interfaces*, 2014, **6**, 15488–15498.

48 B. Z. Fang, Y. L. Xing, A. Bonakdarpour, S. C. Zhang and D. P. Wilkinson, Hierarchical CuO-TiO_2 hollow microspheres for highly efficient photodriven reduction of CO_2 to CH_4, *ACS Sustainable Chem. Eng.*, 2015, **3**(10), 2381–2388.

49 Y. L. Xing, B. Z. Fang, A. Bonakdarpour, S. C. Zhang and D. P. Wilkinson, Facile fabrication of mesoporous carbon nanofibers with unique hierarchical nanoarchitecture for electrochemical hydrogen storage, *Int. J. Hydrogen Energy*, 2014, **39**(15), 7859–7867.

50 Y. Zhang, X. X. Wang, F. Q. Luo, Y. Tan, L. X. Zeng, B. Z. Fang and A. H. Liu, Rock salt type $NiCo_2O_3$ supported on ordered mesoporous carbon as a highly efficient electrocatalyst for oxygen evolution reaction, *Appl. Catal., B*, 2019, **256**, 117852.

51 R. G. He, J. Q. Zhou, H. J. Fu, S. Y. Zhang and C. J. Jiang, Room-temperature *in situ* fabrication of Bi_2O_3/g-C_3N_4 direct Z-scheme photocatalyst with enhanced photocatalytic activity, *Appl. Surf. Sci.*, 2018, **430**, 273–282.